International Journal of Engineering Science 49 (2011) 105–121

Contents lists available at ScienceDirect

International Journal of Engineering Science

journal homepage: www.elsevier.com/locate/ijengsci

Cracks in glass under triaxial conditions

Audrey Ougier-Simonin [a,*], Jérôme Fortin [a], Yves Guéguen [a,**], Alexandre Schubnel [a], Frédéric Bouyer [b]

[a] Laboratoire de Géologie, Ecole normale supérieure, CNRS UMR 8538, 24 rue Lhomond, 75005 Paris, France
[b] CEA Centre de Marcoule DTCD/SECM, Bagnols-Sur-Cèze Cedex, France

ARTICLE INFO

Article history:
Available online 1 August 2010

Keywords:
Glass
Pressure
Damage
Thermal cracks
Elastic parameters

ABSTRACT

This experimental work documents the mechanical evolution of synthetic glass (SON68) under compressive triaxial stresses (hydrostatic and deviatoric conditions). The experimental setup enabled to monitor and vary independently confining pressure (range: [0,50] MPa) and axial stress (up to 680 MPa) at room temperature. An optimized set of sensors allowed us to perform measurements during the experiments of: (i) axial and radial deformation, (ii) *P*- and *S*-elastic wave velocities, and (iii) acoustic emissions. In addition, in some samples, initial crack densities up to a value of 0.24 were introduced by thermal cracking. We compare the original synthetic glass data set to results obtained in the same experimental conditions on thermally cracked glass and on a basaltic rock with similar petrophysical properties (porosity, chemistry).

Stress–strain data depict original linear elastic glass properties even up to an axial stress of 680 MPa (under 15 MPa confining pressure). A strong strength decrease (370 MPa at 15 MPa confining pressure) is observed for thermally cracked samples. Elastic wave velocity data highlight that cracks are mostly closed at a confining pressure of ~30 MPa. The basaltic rock seems to correspond to an intermediate state between an original and a thermally treated glass. In all samples, damage was accompanied by dynamic crack propagation, producing large magnitude acoustic emissions. Thanks to a continuous recorder, we could locate a number of acoustic emissions in order to image the microcracking pattern evolution prior to failure.

1. Introduction

Glass cracking has been, and continues to be a subject of investigation in many fields of fundamental sciences (mechanics and thermo-mechanics, remaining the pioneer work of Griffith in 1920) and of major industrial interests, such as the improvement and the insurance of the nuclear wastes storage. Despite this very large interest of the scientific community, fundamental mechanisms under confining pressure remain unfortunately unclear, and need to be more investigated.

In fact, cracks initiation and growth in brittle solids under tension have been extensively studied by various experimental, theoretical and numerical approaches [3]. It has been established that dynamic brittle fracture is related to fundamental physical parameters and processes, such as crack speed, crack branching, surface roughening, and dynamic instabilities [28–31,11,22]. On the other hand from a fracture mechanics point of view, less studies have been done in the area of compressive fracture despite its vital importance in geology, material science and engineering applications [1,23,24].

* Corresponding author. Tel.: +33 (0)1 44 32 22 09; fax: +33 (0)1 44 32 20 00.
** Corresponding author. Tel.: +33 (0)1 44 32 22 09; fax: +33 (0)1 44 32 20 00.
E-mail addresses: ougier@geologie.ens.fr (A. Ougier-Simonin), gueguen@geologie.ens.fr (Y. Guéguen).

0020-7225/$ - see front matter © 2010 Elsevier Ltd. All rights reserved.
doi:10.1016/j.ijengsci.2010.06.026

One another key point is the impact of thermal cracking which occurs in this material and cannot be avoided, since the synthetic glass is the result of a peculiar process solidification of fused mixed oxides into a canister. Some works performed experimental measurements and theoretical modelling in order to explore thermal crack propagation in glass [21,2,32]. The vitrification process used for nuclear wastes storage and geological disposal has also motivated some thermal cracking investigations in glass [27,35,21,9], but without taking into account a confined pressure.

This is the reason why the present work aims to investigate thermo-mechanical cracking effects on elastic wave velocities and mechanical strength, both under pressure, to evaluate damage evolution on glass. This study has been performed in a triaxial cell on borosilicate glass samples of 80 mm high and 40 mm of diameter at room temperature, without pore fluid pressure. The crack evolution has been monitored with: (i) elastic wave velocity measurements (very sensitive to cracks) and (ii) acoustic emissions (MiniRichter system). We also measured the whole mechanical behavior of our synthetic glass samples with strain gages.

What our study highlights too is the very different behavior of the glass amorphous structure compared to any rock structure. In order to quantify differences between glass and rock, a micro-crystallized basalt sample (Seljadur basalt, Iceland) was chosen with a very low porosity (~5%) and whose composition is as close as possible to the one of synthetic glass. Behavior comparisons were investigated in the exactly same experimental conditions.

Our aim in this article is the behavior description of such samples, as well as synthetic glasses than basalts, with an original methodology based on triaxial cell coupled with the monitoring of the elastic wave velocities. After giving some details in Section 2 about the experiments and the peculiar apparatus modified for the occasion, we apply the whole methodology for investigating elastic wave velocities, cracks measurements and damages behavior in Section 3. Results and all collected data were discussed in Section 4 in order to highlight general trends of glass and basalt mechanical behaviors.

2. Samples, experimental setup and methods

2.1. Samples

We used cylindrical specimens of a borosilicate glass of 80 mm in length and 40 mm in diameter. The chemical composition of the investigated glass is very close to the composition of waste vitrified packages (the SON68 is well known to simulate the present glass composition in the industrial process as shown by Frugier et al. [13]). Platinoids have been included in the glass matrix to simulate the presence of radionucleides of the real vitrified wastes (Table 1). They form insolubles (aggregates, clusters or needles) homogeneously spread within the glass matrix as can be seen in Fig. 1a and b. The glass matrix is amorphous, as expected, with isotropic properties. The porosity is almost close to 0 with a few isolated air bubbles trapped during the glass flow which do not open connectivity into the glass matrix, but may be initial rupture points for cracks propagation.

The starting original material is produced in ideal conditions of slow cooling that prevents any crack formation. A reproducible method was developed in order to be sure to apply the same conditions to any samples we characterize afterwards. Thereby, cracks have been created with an homogeneous distribution and density. All samples have been heated with a furnace (Thermolyne 1400 furnace Sybron©), for which the temperature is controlled with an uncertainty of ±1 °C. An external thermocouple has been added to monitor the temperature of the sample surface. The temperature has been incremented at the rate of 3 °C per minute, up to the maximum chosen heating temperature T_H. The sample was left for 15 h at T_H, then quenched in less than 5 s into distilled water at room temperature $T_A = 20$ °C.

Previous studies on this type of glass revealed that two critical temperatures exist [21]. One is the temperature threshold of 74 °C at which surface cracks appear, the other one is the cracks propagation temperature of 600 °C for which the sample fully breaks into many pieces. In range between 74 and 600 °C, the more is the temperature, the more increase the cracks surface area of the sample. This is the reason why we choose $T_H = 100$, 200 and 300 °C which produce a crack density (responsible for the small porosity of the sample measured by a Hg-porosimeter) of 0.21, 0.23 and 0.24 respectively. The release of the induced stresses produces very fine segmented cracks (see Fig. 1c) on the glass surface. The density and the penetration depth of the crack network increased with T_H. The nucleation sites of the cracks are not clearly identified. It may be nanoscale defects in the matrix or bubbles. However, cracks are definitely independent of the platinoids presence since they do not propagate along the platinoids clusters.

Table 1
Major element composition of the borosilicate glass compared to the basalt used.

	Borosilicate glass (%)	Seljadur basalt (%)
SiO_2	42.73	45.56
Al_2O_3	4.97	16.55
B_2O_3	12.57	–
Na_2O	9.31	2.62
CaO	3.78	13.72
Fe_2O_3	3.10	14.36
Platinoids	1.82	–

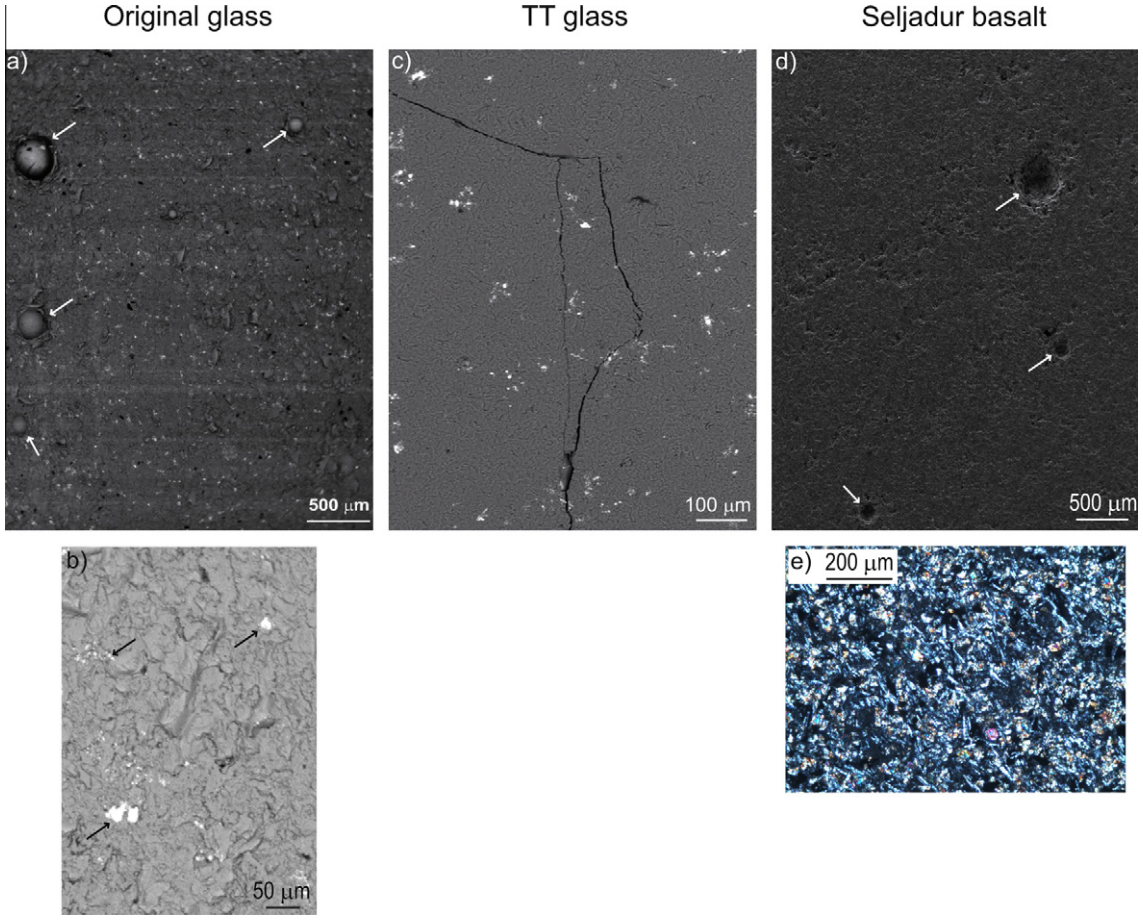

Fig. 1. Natural and synthetic glasses observed through microscopes: (a) scanning electron microscope (SEM) of the original glass texture (general texture with air bubbles indicated by white arrows), (b) zoom on platinoid cluster (indicated by black arrows; zoom on the original glass), (c) SEM of a typical crack in the thermal treated (TT) glass, (d) SEM on Seljadur basalt (white arrows indicate air bubbles), and (e) optical microscope on Seljadur basalt.

The other kind of compound we investigate is a fresh and columnar basalt formed in an intrusive environment, and coming from Seljadur (southwest Iceland). This basalt is composed of plagioclase feldspar and pyroxene with accessory minerals in a microlithic texture [8,42] (Fig. 1e and f). This mineral composition categorises the rock as tholeitic basalt and its chemical composition (Table 1) makes it a good natural analog to the glass that we study. Moreover, it is a compact, high-density rock with porosity of ~5% (of micron sized pores and cracks) and has a permeability of around 10^{-18} m^{-2}. Physical and mechanical properties were studied in the same experimental conditions and compared to the synthetic SON68 glass.

2.2. Experimental setup and methods

Experiments were performed using a triaxial cell installed and upgrade in our laboratory at Ecole normale supérieure in Paris. This apparatus allows for hydrostatic and deviatoric stresses, pore pressure and temperature to be applied independently on a cylindrical specimen (diameter 40 mm × length 80 mm). The pore pressure, the confining pressure and the deviatoric stress can be increased respectively up to 100, 100 and 700 MPa. The isotropic and deviatoric stresses are servo-controlled with an accuracy of 0.01 MPa, and oil is used to confine the whole sample within the cell. All experiments in this work are presented without pore pressure, but it is planned to investigate the influence of a fluid (water) presence on the glass mechanical behavior in the near future. Temperature can be increased up to 200 °C but only room temperature data are reported in this work. This room temperature is controlled with an accuracy of ±0.5 °C around 20 °C. A schematic diagram of the setup is presented in Fig. 2a.

The loading cell allows the use of a maximum of 16 coaxial connections through the wall of the pressure chamber that enable to measure elastic velocities and acoustic emissions, plus 18 single connections for strain measurements. The control and data acquisition are performed by dedicated softwares (Falcon ST© for pressure and strain controls, InSite© for elastic wave velocity measurements, Xstream© for acoustic emission recordings). We used all the signal wires for our experiments.

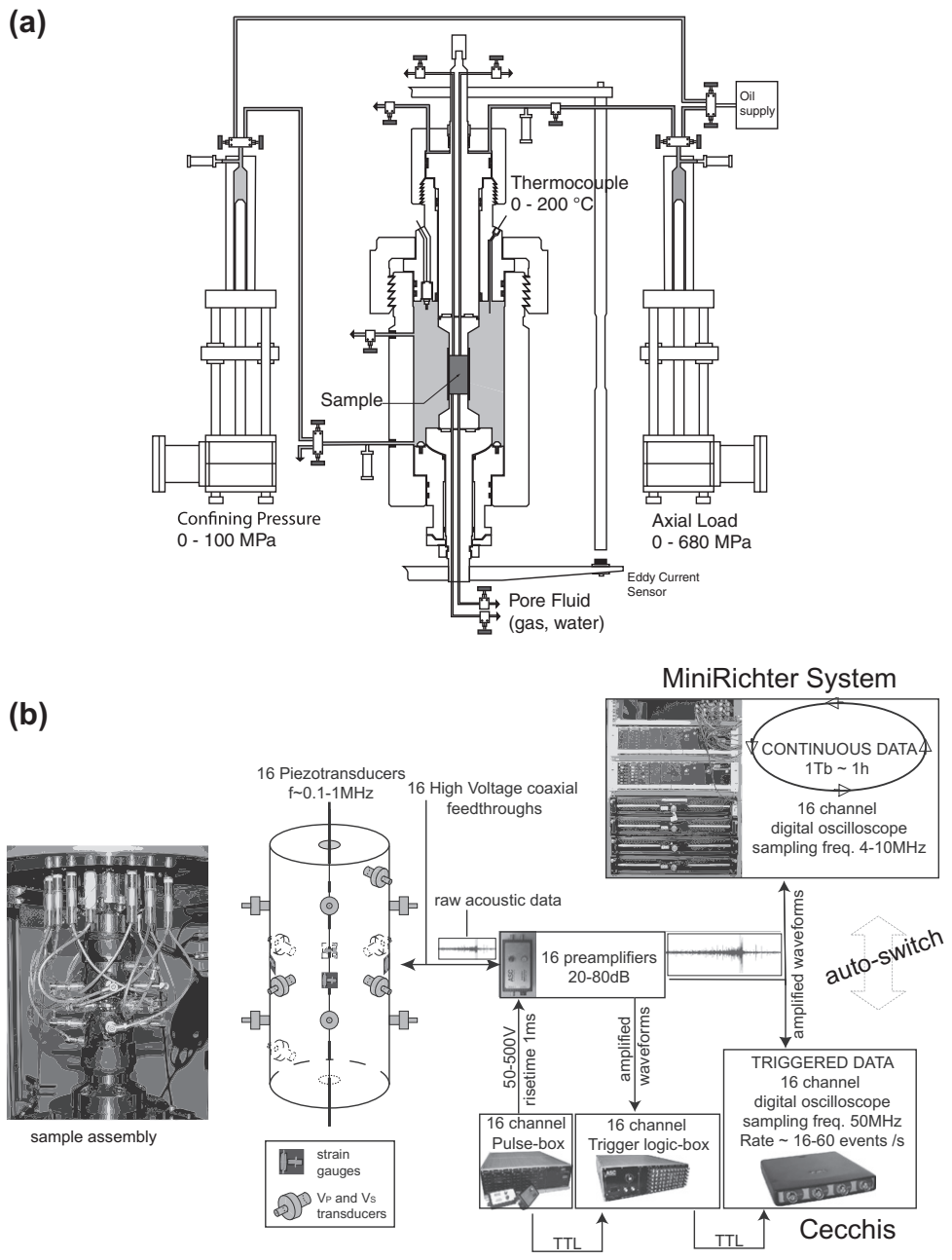

Fig. 2. Schematic diagram of: (a) the axisymmetric triaxial cell and (b) the sensor arrangements around a sample within the triaxial cell.

Eight Tokkyosokki TML FCB strain gages (four axial and four circumferential) of 5 mm long and 120 Ω electrical resistance were glued directly onto the surface sample (Fig. 2b). Each strain gage was used in conjunction with a one-fourth Wheatstone bridge. The measured axial ε_1 and circumferential ε_3 local strains allow for the estimation of the volumetric strain $\varepsilon_v = 2\varepsilon_3 + \varepsilon_1$ and the calculation of the static Young modulus, E_{static}. Axial strain ε_1 and circumferential strain ε_3 were calculated using the average values of the four vertically oriented strain gages and the four horizontally oriented strain gages, respectively. We use the rock mechanic formulation of positive for compressive stresses and strains. The strain gages recorded data every two seconds. An external gap sensor using Foucault currents is used to control the total displacement of the piston during axial loading and provides, once corrected, a global axial strain measurement.

We have also glued directly onto the surface sample 14 ultrasonic piezoelectric transducers (PZTS, Fig. 2b). We used the classical ultrasonic pulse transmission technique for velocity measurements between an emitting and a receiving transducer [4,44]. It consists of measuring the travel time of an elastic pulse through the rock sample for a known travelling path length,

the latter having been corrected for strains during the mechanical loading. The circumferential strain measurement is performed at the half-length of the sample, and the corresponding correction in diameter is applied to radial wave measurements located at the same height and at one third and two thirds of the sample length.

The active electromechanical converter used as compressional (*P*) and transverse (*S*) *P*- and *S*-wave transducers is a PZT (lead zirconate, Polytec PI 255). Radial *P*-waves are generated by 1-mm thick and 5-mm diameter PZTS of 1 MHz central resonant frequency. Axial *P*-waves are generated by 2-mm thick and 10-mm diameter PZTS of 1 MHz central resonant frequency. *S*-waves are generated by 1-mm thick and 5-mm size square PZTS of 1 MHz central resonant frequency with known direction of polarization. Radial *P*-wave PZTS are housed in flat, circular holders (Fig. 2b). Time-delay estimations for all pairs of emitting/receiving transducers are corrected accordingly for the thickness and the nature of the metal support pieces. For the measurement of $V_P^{45^\circ}$ and $V_P^{60^\circ}$, these bronze fitting pieces might introduce some refraction effects resulting from the contrast in elastic impedance between the glass and the bronze ($\Delta Z = 40 \times 10^6$ kg m^{-2} s^{-1}). *S*-wave PZTS are housed in flat, circular aluminum pieces also glued to the sample's lateral face (Fig. 2b).

In active velocity survey mode, a pulse of 250 V with a rise time of 1 μs is generated and transmitted successively to each transducer using a pulsing switchbox (ASC© Ltd.). Each piezoceramic converts this electrical pulse into a mechanical vibration that propagates into the medium. In contrast, each receiving piezoceramic converts the received mechanical waveform into an electrical signal that is amplified at 40 dB using 16 pre-amplifiers. Signals are recorded using a 16 channels Cecchi© digital oscilloscope. Waveforms are sampled at 50 MHz. Velocity surveys were then fully automatically processed using cross-correlation techniques so that the error bar on wave velocity measurements are less than 2%.

This specific arrangement permitted measurements of *P*-wave anisotropy in our sample throughout experiment. These measurements allowed us to identify the two independent isotropic dynamic elastic parameters (Young modulus $E_{dynamic}$, Poisson ratio $v_{dynamic}$) at the start of the experiment and then the five elastic parameters of the transverse isotropy symmetry when the sample was mechanically damaged.

In passive mode, each transducer signal is recorded using the ASC© Ltd. MiniRichter streaming system, which stores continuous ultrasonic waveform data onto a 1 TB hard disk (Fig. 2b). Such continuous recording techniques at this sampling rate have been pioneered in the last years thanks to fast development of computing systems [40,41,38]. Signals were amplified at 40 dB as well. In these conditions, the average electric noise was kept below 15 mV on most channels. The continuous acoustic records were sampled at 4 MHz during 40–70 min (from the first acoustic emission detected until 10 min after failure) providing continuous waveform data on 14 channels. Discrete acoustic emissions (AE) were then harvested after the experiment using a simple triggering technique (300 mV minimum amplitude, 5 μs time window) on these continuous records. Time of first arrivals were automatically picked on each channel for each AE event, using a simple RMS autopicking technique (50 back window, 35 front window, 25 picking threshold). Hypocenter locations were then determinated using a collapsing grid search algorithm, assuming an evolutive medium (from isotropy to transverse isotropy using the velocity model calculated in active mode). The AE hypocenter location were used to determine the origin of the acoustic signals generated during fracturing. Because in our experiment the total number of located AE is significant, we applied a second filter to reduce the number of AE events plotted by only considering AE that were correctly located by seven channels at least. Besides, this second filter prevents from saturated schemes. In such way, AE hypocenter location errors were estimated to be ±2 mm.

All experiments reported here concern dry glass and basalt only (no pore fluid and no temperature field have been applied). The tests were performed applying the same loading–unloading path (Fig. 3): (i) a first part in hydrostatic condition followed by (ii) a second part in deviatoric condition. Firstly, hydrostatic pressure is increased to 50 MPa, then unloaded – after a three minutes stage at 50 MPa – to 15 MPa. The loading rate is 0.01 MPa/s. Each 2.5 MPa, we performed a complete elastic wave velocity survey of the specimen. Secondly, 15 MPa as a confining pressure is applied, which corresponds to a pressure appearing in geological storage conditions around 500 m depth, and deviatoric stress is increased up to failure at a constant strain rate (deformation fixed to 10^{-6} s^{-1}). During this second part, complete elastic wave velocity surveys were performed every 5 min (automatic process).

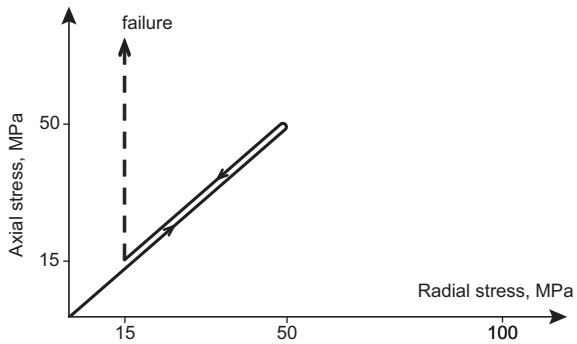

Fig. 3. Stress loading path: (i) hydrostatic conditions (solid line) and (ii) deviatoric conditions (dashed line).

3. Results

A total number of eight samples have been investigated: two samples of the initial glass, two glass samples heated at 100 °C, two samples heated at 200 °C, one sample heated at 300 °C and one basalt sample. Tables 2–4 summarize the physical properties of each type of sample at room conditions, hydrostatic conditions and deviatoric conditions, respectively. For each sample, three data sets were obtained, consisting of a series of strain, elastic wave velocity measurements, and AE recording. Only one example of each type of samples are represented in Figs. 4–7.

3.1. Quasi-static mechanical data

We first examine the quasi-static stress–strain behavior of our samples under hydrostatic conditions (Fig. 4). Both loading and unloading paths are reported and indicated with arrows.

Fig. 4a shows the stress–strain curves of the original and the thermally treated glass samples. For the original glass (black curve with diamond shapes), the volumic strain is linear and very small, with a maximum value of $\varepsilon_v = 0.08\%$ for $P_{hydrostatic} = 50$ MPa. The loading and unloading paths merge, in other words it is reversible.

Both 100 and 200 °C TT samples exhibit an almost linear mechanical behavior (Fig. 4a, black curves with triangle and square shapes). The elastic slope is lower than for the original glass, as expected for cracked samples. They do not exhibit an hysteretic stress strain pattern during loading and unloading. The volumic strain is 0.12% at 50 MPa which is comparable to that of OG. The 300 °C TT sample (black curves with inverse triangle shapes) behaves differently and its mechanical behavior is non-linear. Besides, the mechanical data for this sample were not usable for analysis and interpretation belong $P_{hydrostatic} = 35$ MPa. This might be due to some local strain amplifications on the sample surface close to the strain gages.

Fig. 4b is for the Seljadur basalt (grey curve with circle shapes) compared in the same conditions to the OG. The basalt mechanical behavior is different as it is non-linear. We note a large increase of the volumic strain to 0.6% at 50 MPa confining pressure and a decrease with unloading until 15 MPa (with an hysteresis loop).

Let us focus now on the quasi-static stress–strain behavior of our samples under deviatoric conditions (Fig. 5). Only loading paths are reported here.

Fig. 5a and b shows the mechanical behavior of the original glass (black curves with diamond shapes). When a deviatoric stress is applied, a quasi-linear behavior (axial strain) is observed for the original glass with no dilatancy (Fig. 5c), up to the failure point which occurs at high axial stress (680 MPa for $P_{confining} = 15$ MPa).

The TT plots (Fig. 5a, black curves with triangle and square shapes) exhibit differences from the original glass: (i) the stress–strain plot is not perfectly linear anymore, (ii) the failure point is lower and (iii) dilatancy develops (Fig. 5c). Under deviatoric conditions, all TT samples have a similar mechanical behavior. We observe that the maximum axial stress reached by each TT sample does not correlate in a systematic way to the thermal treatment temperature. In this way, we observe that the failure for the 300 °C TT sample occurs at higher axial stress than for the 100 °C TT sample.

In the same conditions, there is a marked contrast between the original glass and the basalt. The basalt response is less linear (Fig. 5b, grey curve with circle shapes), shows dilatancy (Fig. 5c, grey curve with circle shapes) and its failure point occurs at a lower axial stress (380 MPa for $P_{confining} = 15$ MPa).

Interestingly, we observe small stress drops (indicated by light grey arrows in Fig. 5a and b) previous to the rupture for all glass samples but however not in the basalt.

3.2. Dynamical data

Let us turn to the evolution of elastic wave velocities under hydrostatic conditions (Fig. 6). We only plot the average V_P calculated with the 14 *P*-wave radial and the 2 *P*-wave axial (or 60°) transducers as no anisotropy is observed. V_S is the average measure obtained with the 2 *S*-wave radial transducers. The uncertainty of the values is lower than 2%.

Fig. 6a and b illustrates that in the original glass (black curves with diamond shapes), elastic wave velocities remain constant under hydrostatic pressure. The slight V_P increase up to 10 MPa is probably an experimental artefact due to the transducers adhesion on the glass surface.

Table 2
Elastic parameters measured and calculated at room conditions in the borosilicate glass (original and thermal treated (TT)), compared to the Seljadur basalt ones.

	Original glass	100 °C TT glass	200 °C TT glass	300 °C TT glass	Seljadur basalt
k (%)	0.19	0.21	0.22	0.24	~5
ρ	2.8	2.8	2.8	2.8	2.9
V_P (m/s)	5900–6000	5800–5850	5450–5550	4200–4300	5700–5800
V_S (m/s)	3300–3400	3200–3250	2700–2800	2300–2400	3100–3300
$E_{dynamic}$ (GPa)	82.3–86.9	76.3–79.4	57.2–59.8	41.9–43.7	75.2–84.1
$\nu_{dynamic}$	0.25	0.27–0.28	0.30–0.36	0.32–0.36	0.31–0.33

Table 3
Dynamic Young moduli and Poisson ratio measured in original glass, thermal treated (TT) glass, and basalt, under hydrostatic conditions: $P_{confining}^{loading} = [0, 50]$ MPa.

	Original glass		100 °C TT glass		200 °C TT glass		300 °C TT glass		Seljadur basalt	
$P_{confining}$ (MPa)	0	50	0	50	0	50	0	50	0	50
$E_{dynamic}$ (GPa)	84 ± 0.5		79	81	79	84	78	82	74 ± 0.5	
$\nu_{dynamic}$	0.25 ± 0.5		0.26 ± 0.5		0.29	0.26	0.38	0.29	0.27 ± 0.5	

Table 4
Static and dynamic Young moduli, bulk moduli and Poisson ratio measured in original glass, thermal treated (TT) glass, and basalt, under deviatoric conditions: $\sigma_{axial} = [15, \sigma_{failure}]$ MPa for $P_{confining} = 15$ MPa. Total and selected AE recording are also given.

	Original glass		100 °C TT glass		200 °C TT glass		300 °C TT glass		Seljadur basalt	
σ_{axial} (MPa)	15	680	15	260	15	270	15	330	15	370
E_{static} (GPa)	65.5		71.9		61.3		76.3		53.4	
$E_{dynamic}$ (GPa)	81	70	80	61 ± 5	79	10	57	36 ± 5	73	60
$\nu_{dynamic}$	0.25	0.27	0.27	0.34	0.29	0.4	0.29	0.38	0.27	0.2
Total AE number	96,351		117,255		148,774		134,208		8384	
Selected AE	16,097		11,243		10,474		16,157		970	

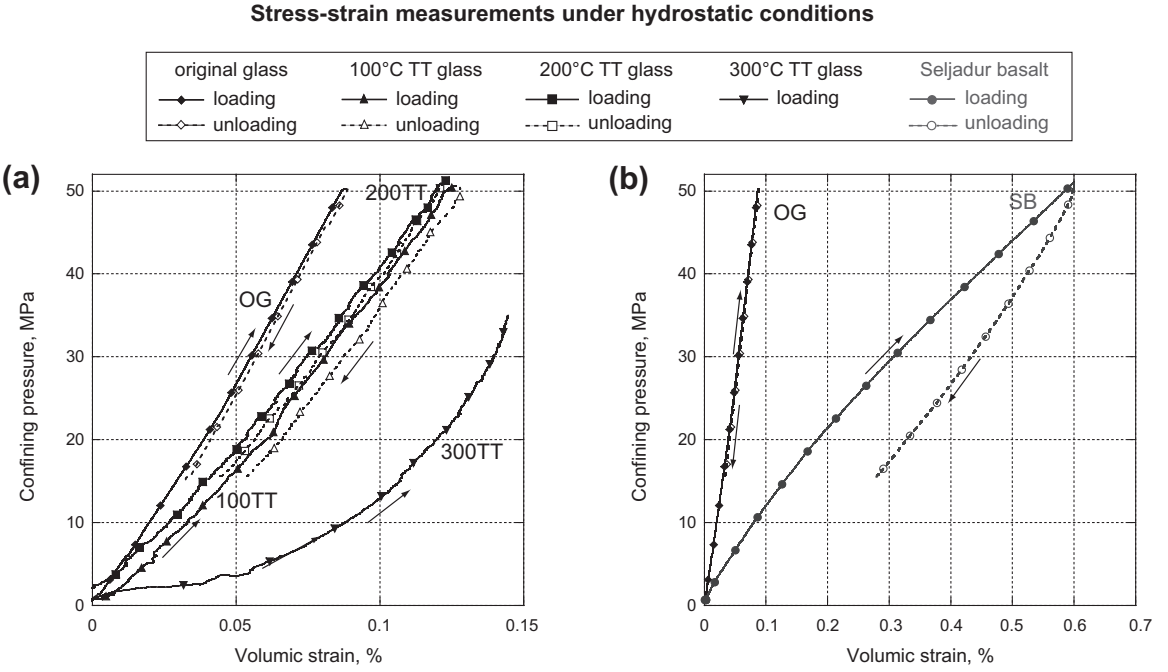

Fig. 4. Stress–strain measurements under hydrostatic pressure: (a) original glass (black curve with diamond shapes, OG) and thermal treated (TT) glasses (black curves with different shapes: 100 TT, 200 TT, 300 TT), and (b) original glass (black curve with diamond shapes, OG) and basalt (dark grey curve with circle shapes, SB).

The influence of the thermal treatment is clearly seen on the elastic wave velocity measurements (Fig. 6a). As expected, the more is the temperature of thermal treatment, the less are the velocities values (black curves with triangle and square shapes). As the hydrostatic pressure increases, the elastic wave velocities raise to reach a similar state as the original glass one (at around 30 MPa confining pressure for the 100 and 200 °C TT samples).

The basalt velocities (Fig. 6b, dark grey curves with circle shapes) also remain stable under the same hydrostatic conditions despite the very small decrease observed for confining pressure from 0 to ~15 MPa.

The evolution of the elastic wave velocities under deviatoric conditions is clearly different as shown in Fig. 7. Only V_{Paxial} and $V_{Pradial}$ for each type of samples are reported here. The average $V_{Pradial}$ is calculated with the 14 *P*-wave radial transducers and the average of V_{Paxial} is calculated with 2 *P*-wave axial (or 60°) transducers. Both Fig. 7a and b represent the decreasing of the elastic wave speeds when increasing deviatoric stress.

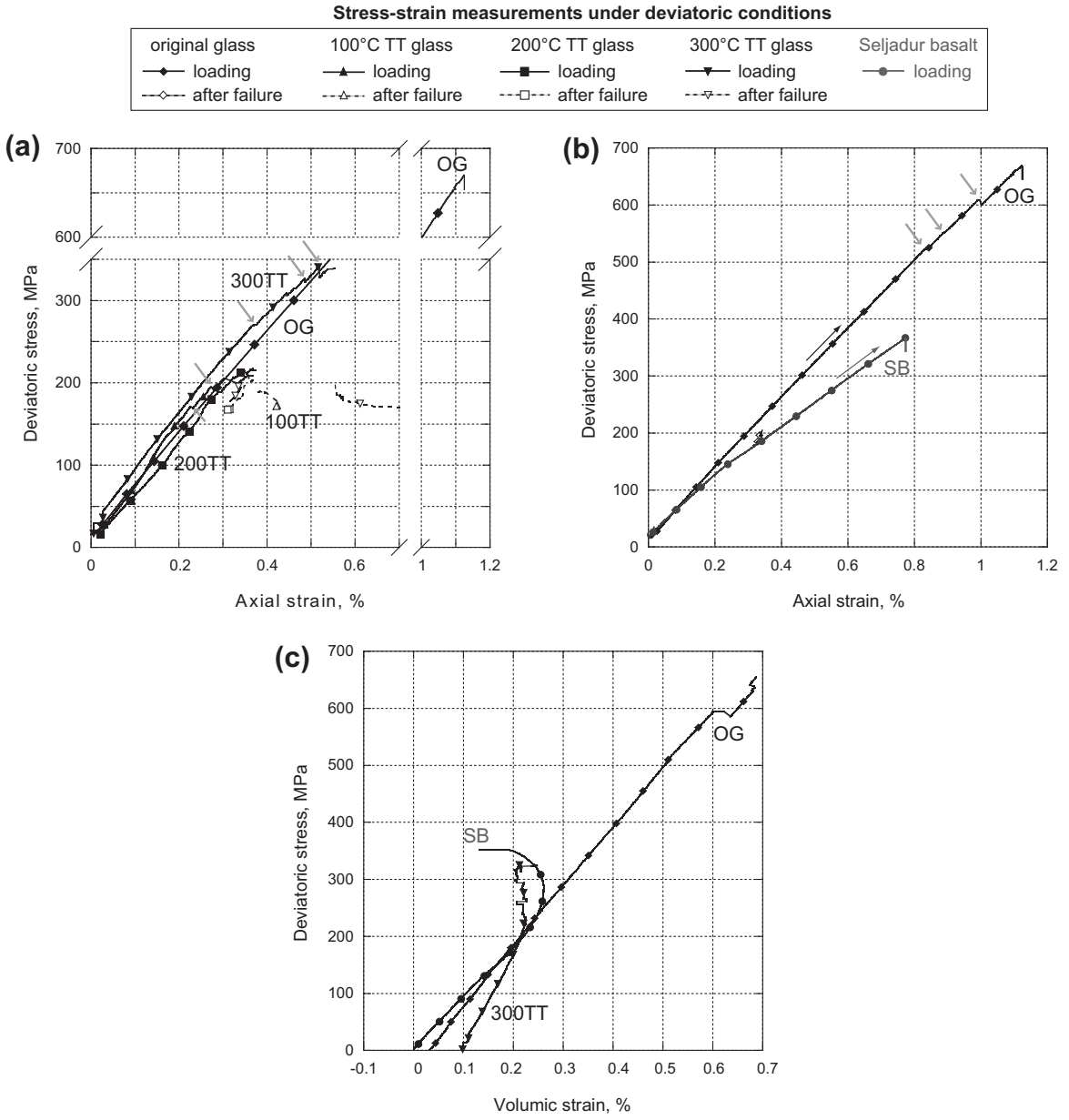

Fig. 5. Stress–strain measurements under deviatoric conditions: (a) original glass (black curve with diamond shapes, OG) and thermal treated (TT) glasses (black curves with different shapes: 100 TT, 200 TT, 300 TT) and (b) original glass (black curve with diamond shapes, OG) and basalt (dark grey curve with circle shapes, SB). Dilatancy effect is plotted in (c) for original glass (OG), 300 °C TT glass (300 TT) and basalt (SB).

Considering the original glass (Fig. 7a, black curve with diamond shapes), both V_{Paxial} and $V_{Pradial}$ remain stable up to $\sigma_{axial} \sim 400$ MPa. From $\sigma_{axial} \sim 400$ MPa up to the failure point, V_{Paxial} slightly increases first then slightly decreases, while $V_{Pradial}$ decreases significantly. This fact is directly related to the increasing damage developing in the sample. The anisotropy is calculated as follow: $A = (V_{Paxial} - V_{Pradial})/V_{Paxial}$, and attests its minor effect as depicted in Fig. 7c.

However, all TT glasses record important $V_{Pradial}$ drops from $\sigma_{axial} = 100$ MPa up to failure. More precisely, TT glass $V_{Pradial}$ decreases drastically up to failure as V_{Paxial} remains stable in comparison ($V_{P,axial} = 5950 \pm 50$ m/s) excepted for the 300 °C TT sample (black curves with triangle shapes). In this case, V_{Paxial} also decreases significantly from $\sigma_{axial} \sim 200$ MPa up to failure. As a consequence, the anisotropy A for TT glass samples increases considerably with axial stress (Fig. 7c).

The damage in the basalt is isotropic since both V_{Paxial} and $V_{Pradial}$ show similar decreasing velocities (similar slope for dark grey curves with circle shapes in Fig. 7b). So, the anisotropy remains close to zero with increasing σ_{axial} (Fig. 7c); this might be related to the intrinsic properties of the basalt.

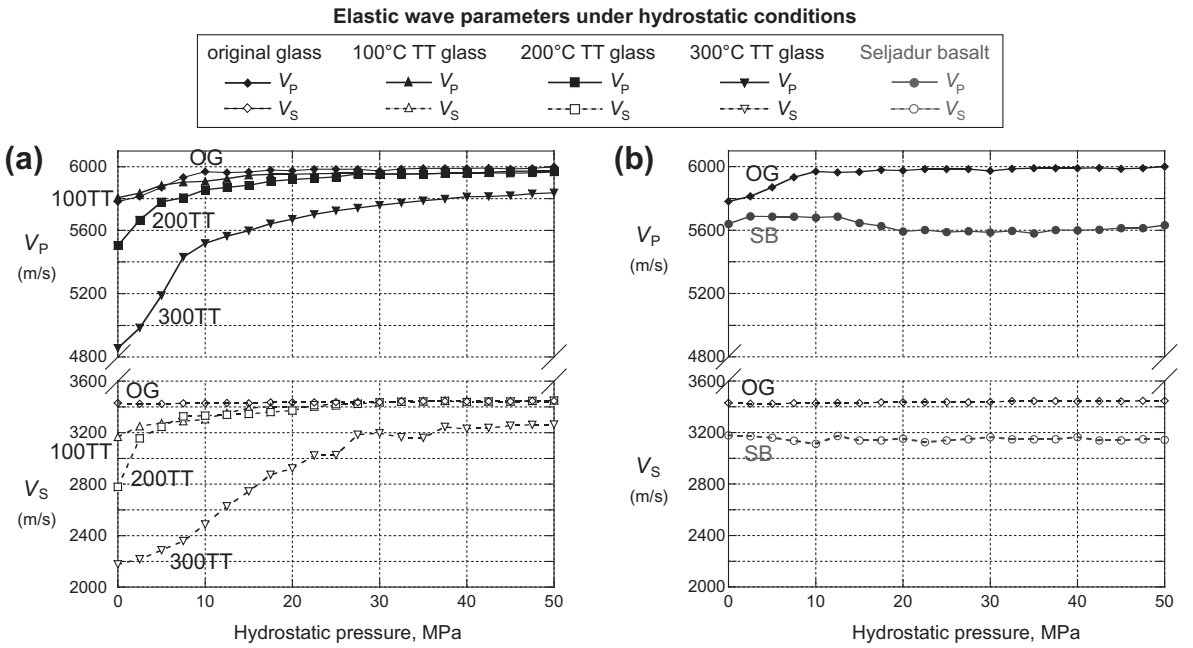

Fig. 6. Elastic wave velocity measurements (V_P and V_S) obtained under hydrostatic conditions: (a) original glass (black curve with diamond shapes, OG) and thermal treated (TT) glasses (black curves with different shapes: 100 TT, 200 TT, 300 TT), and (b) original glass (black curve with diamond shapes, OG) and basalt (dark grey curve with circle shapes, SB).

3.3. Acoustic emissions (AE)

AE monitoring was performed during the deviatoric loading. The numbers of AE events identified and selected are given in Table 4. Fig. 8b, d and f shows the localized events (represented by small circles) occurring at ±2 s around the indicated time. These events correspond to the spikes in Fig. 8a, c and e. It is important to point out that all these events depict the localization of the cracks or their propagation, but not a continuous fracture itself. What is highlighted is the AE activity in those glasses, which is very significant and not specifically correlated to the thermal treatment. The AE rate at the onset of failure is largest for OG sample and reaches a rate of 10,000 events per 4 s, while only about 1000 for the TT sample presented and 3500 for the basalt sample. In fact, an average total amount of 120,000 AE were sampled for each experiment (original and TT glass). We present only the best located AE events to enhance the visiblity of the recorded phenomena (Fig. 8).

In the original glass, AEs cluster in two principal swarms which are close to the sample ends (Fig. 8b-1). With increasing deviatoric stress the AE event rate and major events (AE rate spikes) increase (Fig. 8a). AE events migrate from the ends to the middle of the sample with increasing axial stress (Fig. 8b-2 and b-3). We observe that AE rate spikes are correlated with small stress drops. Finally, the two principal clusters combine into a quite homogeneous axial cluster which drives the failure and gives an idea of the major crack geometry. At the end, that is when the sample block is fractured, the AE rate is recorded to its maximum (major spike in Fig. 8a and b).

Fig. 8c represents one TT glass which is definitely representative of the difference between the original and the thermal treated glasses. We observe that the AE rate start to be more significant at a stress lower than for the original glass (Fig. 8b and d). The first AE events thus seem to correspond to the activity of cracks probably created by the thermal treatment. The orientation of the principal cluster is not driven by the axial stress (Fig. 8d-1). At higher σ_{axial}, the AE events localize the damage principally in the middle of the sample, mostly parallel to the axial stress (Fig. 8d-2). It seems that the mechanical damage becomes higher than the damage caused by the thermal treatment. Finally, the failure point results from the coalescence of all AE clusters. The total damage is distributed in several orientations. We note again that AE rate spikes fit with small stress drops which occured during the loading.

AE rate recorded in the basalt is quite different (Fig. 8e). AE only occured just before macroscopic failure of the specimen. Two clouds of AE events develop at an angle of ~45° from the axial stress. This observation is in good agreement with the V_P evolution under axial stress and with the resulting V_P zero anisotropy (Fig. 7b and c).

4. Discussion

Considering Tables 2 and 3, the effect of cracks seems to be obvious from the first thermal treatment. Elastic wave velocities have lower values and the dynamic Young moduli are decreasing at the same time. As the density remains stable, the

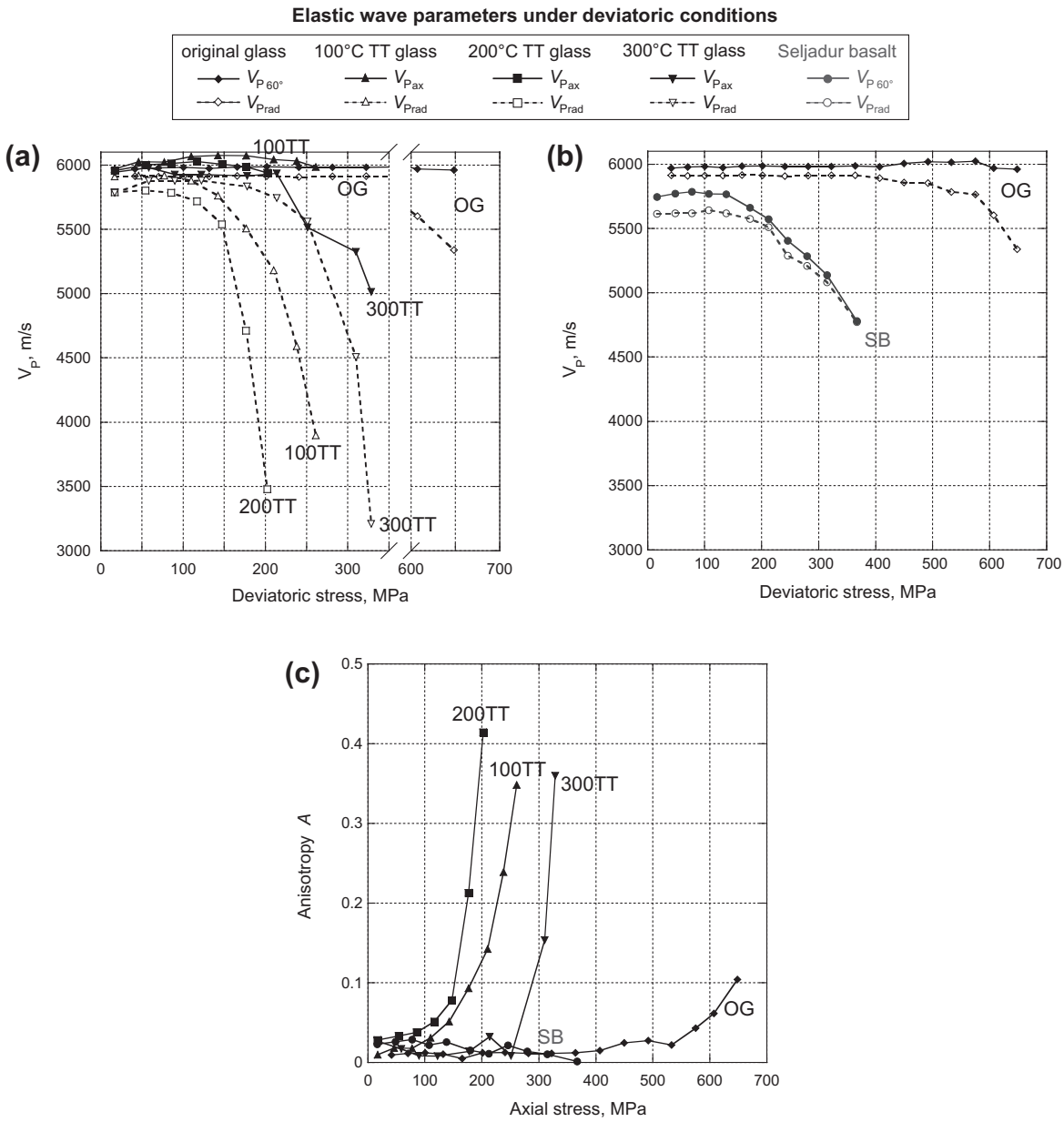

Fig. 7. Axial (V_{Paxial}) and radial ($V_{Pradial}$) elastic wave velocity measurements obtained under deviatoric conditions for 15 MPa confining pressure: (a) original glass (black curve with diamond shapes, OG) and thermal treated (TT) glasses (black curves with different shapes: 100 TT, 200 TT, 300 TT), and (b) original glass (black curve with diamond shapes, OG) and basalt (dark grey curve with circle shapes, SB).

porosity remains very low and it suggests that the cracks produced by the thermal treatment have a very small aspect ratio. The Seljadur basalt seems to correspond to an intermediate state between an original and a damaged glass as its elastic parameters fit glass data in-between. The discussion focuses on the effect of pressure on these first results.

The elastic waves are very sensitive to the presence of cracks (Fig. 7) [43,17,12]. Because damage in glass is due to cracks, we analyse our data using the model of Kachanov [20] that appears to be appropriate for an elastic solid with many cracks. Such a method has been successfully applied to different cracked rocks (sandstones, granites, shales) as shown by several authors [36,37,10,34]. We estimate the crack density using the average of Eqs. (2) and (3) of the Appendix for isotropic case (original glass and basalt), and Eq. (5) when anisotropy cannot be neglected (thermally treated glass), as given in Appendix. We point out that the crack density parameter ρ_c is not defined for the realistic, 'irregular' crack shapes. This difficulty is partially overcome by the fact that any distribution of irregularly shaped cracks is equivalent to certain distribution of circular cracks [15] if the cracks are flat (planar) even if some of them intersect (provided the material remains coherent,

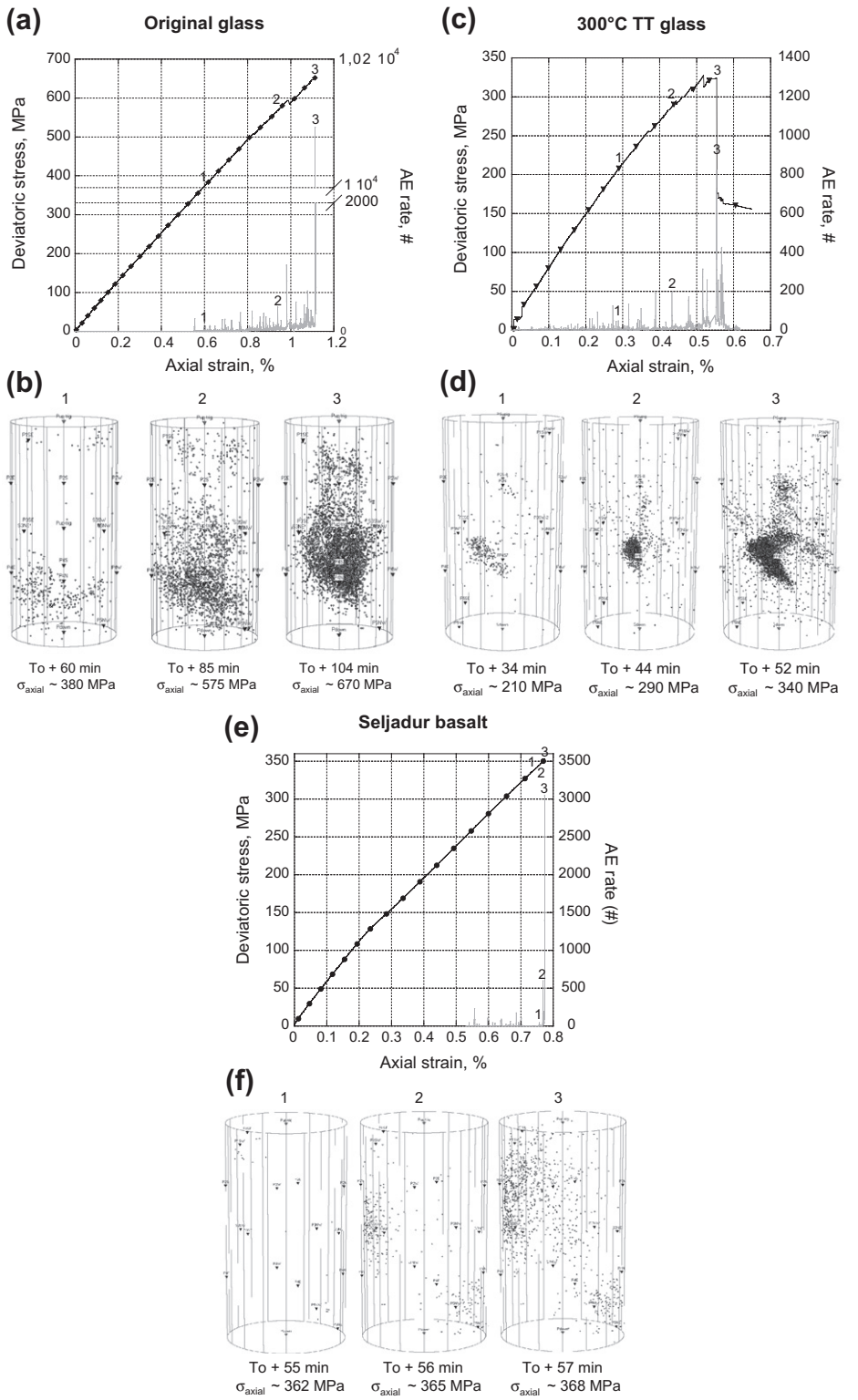

Fig. 8. Location of AE and correlation between AE rate and deformation during deviatoric loading ($P_{confining}$ = 15 MPa). In graphics (b), (d) and (f), we plot in virtual samples the localized events (represented by small circles) occurring at the indicated time. These events correspond to the AE rate picks in graphics (a), (c) and (e).

overall). Hence the crack density parameter ρ_c can be retained in such cases. However, finding the value of ρ_c, i.e. the density of the equivalent distribution of circular cracks, requires knowledge of compliances of irregularly shaped cracks. Although certain progress has been made in this direction [39,15], further work is needed.

4.1. In hydrostatic conditions

The quasi-static behavior of the original glass is clearly linear elastic under hydrostatic conditions ($P_{confining}^{loading} = [0, 50]$ MPa and $P_{confining}^{unloading} = [50, 15]$ MPa), as reported in Fig. 4. The loading and unloading paths overlap over more than 90%. V_P and V_S values remain stable (Fig. 6) and as a consequence the crack density is almost equal to 0 during the loading (Fig. 9). We note again that the small increase of V_P value at the beginning of the hydrostatic measurements is an experimental artefact. Assuming the uncertainty due to the experimental conditions (signal source sensor distances, *P*-wave arrival picking), we measure for the original glass: $V_P = 5970 \pm 30$ m/s, so $E_{dynamic} = 84$ GPa and $\nu = 0.25$ (Table 3). We note that the dynamic Young modulus in hydrostatic condition is isotropic.

Considering the TT glasses (Figs. 4a, 6a and 9), the effect of initial thermal damage on the material is clear: the volumic strain for TT glasses of thermal treatment temperature lower than 200 °C remain close to the original glass one (see Fig. 4a). The loading and unloading paths do not overlap but have the same slope. As the hydrostatic pressure increase, the low pressure V_P and V_S values for the TT glass increase to reach the average value measured on the original glass for $P_{confining} \sim 30$ MPa (cf. Fig. 6a). The initial V_P and V_S values for the TT samples are directly related to the thermal treatment temperature: they decrease as the thermal treatment temperature increases. We follow this process in Fig. 9 with the decrease of the crack density corresponding to all TT samples. An exception is the sample thermally heated to 300 °C which behaves significantly in comparison to the other treated glass samples. The corresponding dynamic Young moduli are between $78 < E_{dynamic,TT} < 84$ GPa (Table 3) and depict an isotropic material even with the thermal treatment (these values are very close to the OG one, $E_{dynamic,OG} \sim 84$ GPa).

At the beginning of the loading, the increasing V_P and V_S values correspond to crack closure under hydrostatic pressure [43,25]. From the crack closure stress σ_{cl}, the mean crack aspect ratio ξ can be estimated with the following equation [43]:

$$\sigma_{cl} = \frac{E\xi}{2(1-\nu^2)},$$

where ν is the Poisson ratio, and E the Young modulus. For the 100 and the 200 °C TT samples, using $\sigma_{cl} = 15$ MPa, we estimate $\xi_{100TT,200TT} \sim 10^{-4}$ with $E = E_{dynamic,100TT} = 80.7$ GPa, $E = E_{dynamic,200TT} = 82.1$ GPa, $\nu_{100TT} = 0.27$ and $\nu_{200TT} = 0.26$. These crack aspect ratios are in good agreement with the thermal damage controlling scale in this type of material [32]. However, thermal cracks created by a thermal treatment temperature lower than 200 °C seems to have a very small effect on the elastic velocities. The most important effect is for the sample thermally shocked at 300 °C. In this case, we calculate $\xi_{300TT} \sim 10^{-3}$ for $\sigma_{cl} \sim 40$ MPa, $E = E_{dynamic,300TT} = 29.85$ GPa and $\nu_{300TT} = 0.44$, which fit well with our data.

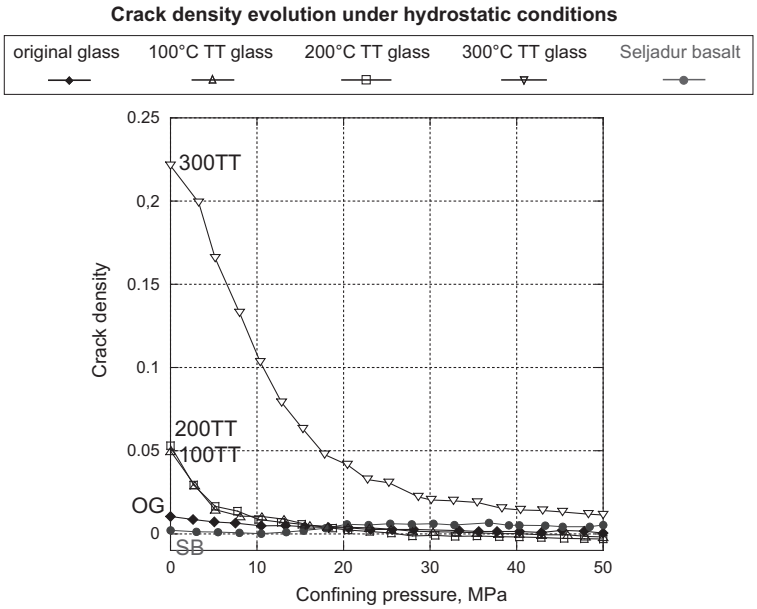

Fig. 9. Crack density evolution under hydrostatic conditions of the original glass sample, the TT glass samples and the natural analog (Seljadur basalt).

In contrast, the quasi-static behavior of the basalt sample exhibits a clear hysteresis (Fig. 4b). This effect is due to irreversible local deformation. This is in agreement with the slight V_P decrease observed for basalt at 20 MPa (Fig. 6b). It might be interpreted as local pore collapse associated with local cracking and/or sliding cracks [43,18,7]. It suggests that the basalt contains a few pores (bubbles) but almost no cracks and have a quasi isotropic texture. This is in agreement with the work of Vinciguerra et al. [42] on the same basalt. It fits with the almost zero mean crack density calculated for an isotropic medium by inverting the corresponding elastic moduli K and G (Fig. 9) (see Appendix). Finally, the basalt seems to correspond to an intermediate state between an original and a damage glass in hydrostatic conditions as it has a non-elastic mechanical behavior but isotropic elastic dynamical parameters.

4.2. In deviatoric conditions

Beyond a critical axial stress, Figs. 5, 7 and 8 show cracks initiation and propagation leading to the sample fracture. The increasing crack density is clearly seen through the reduction of V_P (and V_S) values. It can also be followed through the evolution of the crack density (Fig. 11). This reduction is more significant on the radial V_P measurements than on the axial V_P measurements for all glass samples (Fig. 7). It suggests that cracks developed preferentially along the axis of principal stress, the vertical axis following the schematic pattern illustrated by Fig. 10. The increasing anisotropy highlights this effect when increasing pressure, in particular for the TT samples Fig. 7c).

We would like to point out that the original glass mechanical behavior remains very elastic despite the increasing damage (Figs. 6 and 7). During the loading, small stress drops (indicated by light grey arrows in Fig. 5a) can be seen just before the rupture. They may correspond to significant crack nucleation and/or propagation in our sample as we recorded about 96000 AE during these 70 min of deviatoric experiment (Table 4). The elastic wave velocities recorded in the same time show a first stable part with both V_{Paxial} and $V_{Pradial}$ values equal to 5970 ± 30 m/s. At $\sigma_{axial} \sim 400$ MPa, the induced cracks start to be significant as the velocities decrease (Fig. 7a) and the anisotropy A starts to increase (Fig. 7a and c). The rupture occured at 680 MPa of axial stress (for $P_{confining} = 15$ MPa) and at almost 1.2% axial strain. At this critical point, the axial stress drops

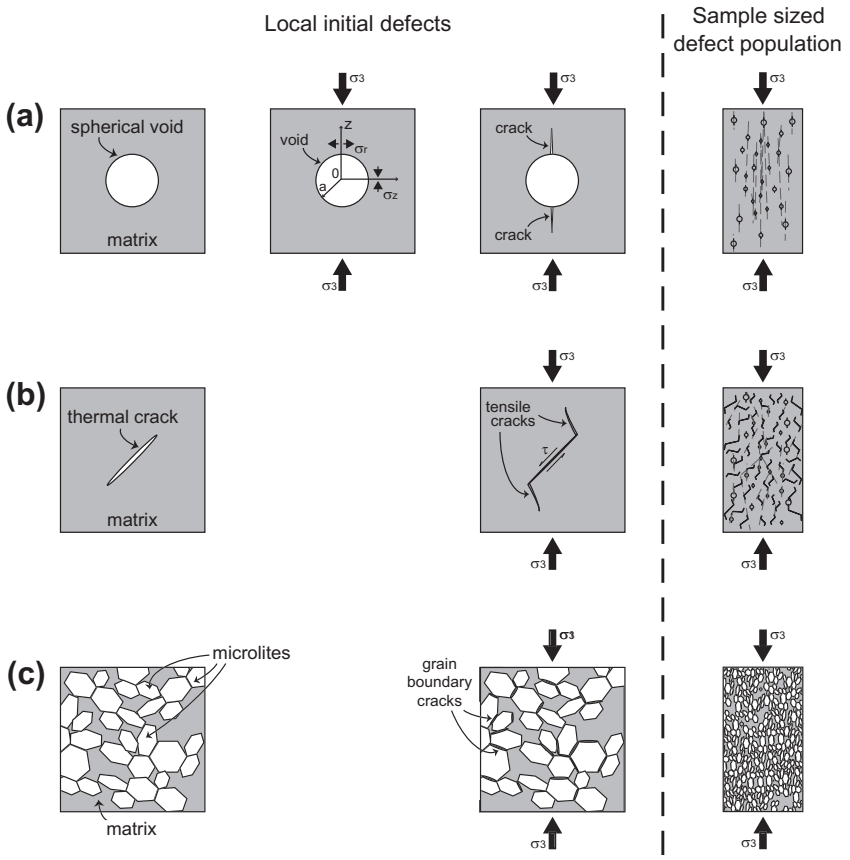

Fig. 10. Mechanisms of compressive failure in a schematic fashion: (a) case of the original glass with only spheroidal default identified (air bubbles), (b) case of the TT glass with preexisting thermal cracks in the glass matrix, and (c) case of the Seljadur basalt with microlites in a siliceous matrix. We assume in this schematic model that $\sigma_3 \ll \sigma_1$.

to 200 MPa occurs in less than 1 s. Considering both anisotropic and AE data, we deduce that the rupture orientation is parallel to the deviatoric stress. It results in a global crack connection with two initial clusters (Fig. 8) along this preferential orientation. Whereas ductile metals can tolerate large compressive strain without failure, flaws are generated under compressive stresses [26] in brittle materials (ceramics, rocks, glasses, etc.). Spherical voids lead to tensile stresses when samples are loaded in compression [14,33]. As the original glass is exempt from any cracks previous to the experiment, it might be the air bubbles trapped during glass cooling which initiate the damage. This process is schematically illustrated in Fig. 10a. Cracks induced by the deviatoric stress are expected to be mainly vertical. Let us turn to the TT glasses (Fig. 5a). We first note that despite the thermal treatment and the mechanical damage, all samples exhibit an almost linear elastic behavior under deviatoric stress up to failure. We also note that the failure point occurs in a range of axial stress ($\sigma_{axial,TT}$ = [200, 350] so $\sigma_{axial,TT} \ll \sigma_{axial,OG}$) and not at a critical value which would be uniformly correlated to the maximum heating temperature of the thermal treatment. The mechanical damage which develops in the elastic domain is due to cracking. With increasing deviatoric stress, radial V_P decreases drastically and, as expected, anisotropy develops and reaches a high value for all the TT samples just before failure (Fig. 7c). This is illustrated in Fig. 8 (300 °C TT glass data) where point 1 (200 MPa axial stress) shows non-vertical AE clusters (probably thermal cracks) and points 2 and 3 (close to 300 MPa axial stress) show axial AE clusters (probably mechanically induced vertical cracks). Assuming transverse isotropy [36], observed elastic wave velocities are inverted in terms of crack densities (Fig. 11). The velocity anisotropy values reach about 40% just before the sample failure. Corresponding total crack densities ($\rho_c = 2\alpha_{11} + \alpha_{33}$) at the same point reach about 0.3. Note that the dynamic Young moduli $E_{dynamic}$ of these TT samples are also anisotropic as $E_{axial} \neq E_{radial}$. This explains the variations of $E_{dynamic}$ value in Table 4 during the experiments. A significant difference in these $E_{dynamic}$ values is calculated for the 300 °C TT glass in comparison to the 100 °C TT and 200 °C TT glasses (Table 4). Finally, the range of failure axial stresses of the TT glass sample seems to depend only of the existence of thermal crack and not of the maximum heating temperature of the thermal treatment. It has been suggested by Gross et al. [16] that the oscillatory instability of crack tip beyond a threshold velocity is a generic feature of fracture in brittle amorphous materials. Short time scale processes near the crack tip consumed most of the fracture energy and the amount of AE represents almost the whole fracture surface structure, that is the cracks network topology. The resulting anisotropy of the elastic wave velocities shows that the anisotropic mechanically induced cracks dominate over the initial thermal cracks which are randomly oriented (Fig. 10b).

For the basalt, both radial and axial V_P measurements recorded almost the same increasing damage (Fig. 7b and c). The mechanical behavior changes from a first elastic part (between 0 and 100 MPa of axial stress) to a clearly non-elastic part as dilatancy develops from $\sigma_{axial} \sim 200$ MPa up to failure (Fig. 5b). Besides, in comparison to the glass, the basalt produced fewer AE (less than 10,000). Two clusters seem to be concentrated in one zone at about 45° from the horizontal (Fig. 8f-2) and oriented the general damage. Moreover, all the damage appear at the end of the loading (Fig. 11). It underlines that cracks distribution is isotropic. Microlite boundary cracking (due to differences of elastic properties between microlites) seems dominating and playing an important role for the basalt, so that it develops an preferred orientation which is completely different from the axial stress (Fig. 10c).

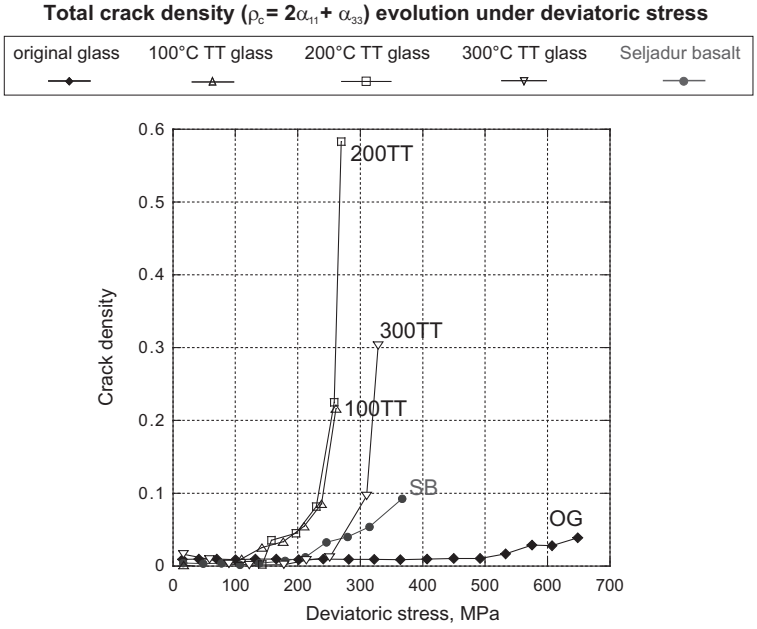

Fig. 11. Crack density evolution under deviatoric stress for a confining pressure of 15 MPa of the original glass sample, the TT glass samples and the natural analog (Seljadur basalt).

Interestingly, we observe small stress drops (indicated by light grey arrows in Fig. 5a) previous to the rupture for all glass samples but however not in the basalt. This effect might be correlated to crack arrest in the glass samples before the macroscopic failure.

5. Conclusions

We investigated (thermo-)mechanical cracking effects in glass on elastic wave velocities and mechanical strength, both under pressure. Using AE recording in addition, we have obtained several data set on glass cracking under deviatoric stress. In our experiments, we observe: (i) an almost perfect linear elastic behavior of the original glass under pressure, (ii) a strong influence of the thermal treatment on glass failure strength, and (iii) a variable influence of the thermal treatment on glass elastic properties (minor if $T_H \leqslant 200$ °C, major if $T_H \geqslant 200$ °C).

Data set analysis points out the development of previously initiated cracks. Crack orientation is controlled by the main principal compressive stresses. This is generally observed even for glass with initial thermal cracking. From crack velocities data, axial crack density exceeding 0.5 are recorded just before failure while AE events are recorded since the beginning of the axial loading. Cracks aspect ratio are in the range of $[10^{-4}, 10^{-3}]$.

Despite some differences between rock and glass, basalt remains an interesting natural analog. Further works will focus on permeability measurements in order to quantify the impact of cracking on this transport property. Such data would be of crucial interest for application in the field of vitrified nuclear waste under geological storage conditions. As glass is an almost ideally brittle elastic material, they are also of fundamental interest to investigate fracture mechanics under pressure.

Acknowledgments

This research work has been initiated by the French Atomic Energy Commission (CEA), and supported by AREVA NC and l'ANDRA (French National Radioactive Waste Management Agency). They are gratefully acknowledged for their fruitful discussions and advice. We are grateful to the help of the CEA laboratory for providing all SON68 samples. We would like to thank Yves Pinquier and Thierry Decamps for their technical support. We also thank Pr. Philipp Meredith and Dr. Mike J. Heap for providing us with Seljadur basalt. Finally, we would like to acknowledge Dr. Will Pettitt of ASC© Ltd. for his crucial help in setting up the acoustic recorder system.

Appendix. Crack density modelling

Cracks may strongly affect the overall elastic properties, in spite of the fact that they have small opening (aspect ratio) so that the 'crack porosity' is negligible. Moreover, aspect ratios do not matter as long as they are below 0.10–0.12 (see, for example, [19]). The usual measure of crack density – defined for the circular (penny-shaped) cracks – introduced by Bristow [5] is

$$\rho_c = 1 \Big/ V \sum_{i}^{N} a_i^3, \tag{1}$$

where a_i is the radius of the ith crack and N is the total number of cracks in the representative elementary volume (REV) V. It has been generalized by Budiansky and O'Connell [6] to planar elliptical cracks (and expressed explicitly in terms of ellipse parameters). In cases of overall isotropy, the effective elastic constants were given, in the non-interaction approximation, by Bristow [5] and, in the context of rock mechanics, by Walsh [43]:

$$\frac{K_o}{K} = 1 + \rho_c \frac{h}{1 - 2\nu_o}\left\{1 - \frac{\nu_o}{2}\right\}, \tag{2}$$

$$\frac{G_o}{G} = 1 + \rho_c \frac{h}{1 + \nu_o}\left\{1 - \frac{\nu_o}{5}\right\}. \tag{3}$$

K is the effective bulk modulus which can be directly inverted from a combination of the P and S wave velocities and G is the effective shear modulus which can be directly inverted from the S wave velocities. K_o and G_o are the bulk and shear moduli of the crack-free matrix, and ν_o the corresponding Poisson ratio of this state. h is a factor given by

$$h = \frac{16(1 - \nu_o^2)}{9(1 - \nu_o/2)}. \tag{4}$$

However, cracks in brittle materials typically have highly irregular shapes (non-elliptical, intersecting, non-planar), for which the parameter (1) is not defined. If one wishes to use crack density as a micromechanical – rather than fitting – parameter, the effect of these shape irregularities needs to be quantified and this constitutes the main difficulty in application of the present model. Certain progress has been made in this direction.

In a more general case when the orientation distribution is not isotropic, the overall moduli cannot be expressed in terms of ρ_c only. For a unified coverage of non-random orientations, a second rank tensor $\boldsymbol{\alpha}$ is substituted for the scalar crack density ρ_c

$$\boldsymbol{\alpha} = \frac{1}{V}\sum (a^3 \mathbf{nn})^i, \tag{5}$$

where $\mathbf{n}$ is a unit normal to a crack and $\mathbf{nn}$ is a dyadic product. The linear invariant $\alpha_{kk} = \rho_c$ so that $\boldsymbol{\alpha}$ is a natural tensorial generalization of ρ_c. The fourth rank tensor

$$\boldsymbol{\beta} = \frac{1}{V}\sum (a^3 \mathbf{nnnn})^i \tag{6}$$

was identified as a second crack density parameter [20]. But it plays a relatively minor role in the dry case which is the case of this paper. We consider a general transversely isotropic orientation distribution of cracks which is realistic for the thermal treated glasses under deviatoric stress, Ox_3 being the axial compressive stress direction. So, $\alpha_{11} = \alpha_{22} \neq \alpha_{33}$ and $\boldsymbol{\beta}$ is neglected. The elastic moduli C_{IJ} (Voigt two-index notation) depend on α_{11} and α_{33}. The moduli are obtained from anisotropic *P*- and *S*-wave velocities. We give the simplified relations we used:

$$C_{11} + C_{12} = \frac{S^o_{11} + \alpha_{33}}{D}, \tag{7}$$

$$C_{33} = \frac{S^o_{11} - S^o_{12} + \alpha_{11}}{D}, \tag{8}$$

$$C_{44} = \frac{1}{2S^o_{11} - 2S^o_{12} + \alpha_{11} + \alpha_{33}}, \tag{9}$$

$$C_{13} = \frac{-S^o_{12}}{D}, \tag{10}$$

$$C_{66} = \frac{1}{2S^o_{11} - 2S^o_{12} + 2\alpha_{11}}, \tag{11}$$

where

$$D = \left(S^o_{11} + \alpha_{33}\right)\left(S^o_{11} + S^o_{12} + \alpha_{11}\right) - 2\left(S^o_{12}\right)^2, \tag{12}$$

and $\mathbf{S}^o$ is the matrix compliance tensor defined as $\mathbf{S}^o = \mathbf{C}^{o-1}$. In particular, we reduce the number of elastic parameters to calculate the crack density to Eqs. (7) and (8) as our best experimental measurements give us C_{11}, C_{12} and C_{33}. This reduction of initial input parameters in our model introduces an error on the crack density value at 10^{-3} order.

References

[1] M. Adda-Bedia, M.B. Amar, Stability of quasiequilibrium cracks under uniaxial loading, International Journal of Fracture 76 (1996) 1497–1500.
[2] M. Adda-Bedia, Y. Pomeau, Crack instabilities of a heated glass strip, Physical Review E 52 (1995) 4105–4113.
[3] T. Anderson, Fracture Mechanics, second ed., CRC Press, New York, 1995.
[4] F. Birch, The velocity of compressional waves in rocks to 10 kilobars, Journal of Applied Mechanics 65 (1960) 1083–1102.
[5] J. Bristow, Microcracks and the static and dynamic constants of annealed and heavily cold-worked metals, British Journal of Applied Physics 11 (1960) 81–85.
[6] B. Budiansky, R. O'Connell, Elastic moduli of a cracked solid, International Journal of Solids and Structures 12 (1976) 81–97.
[7] C. David, B. Menendez, J.-M. Mengus, Influence of mechanical damage on fluid flow patterns investigated using ct scanning imaging and acoustic emissions techniques, Geophysical Research Letters 35 (2008) L16313.
[8] D. Eccles, P. Sammonds, O. Clint, Laboratory studies of electrical potential during rock failure, International Journal of Rock Mechanics and Mining Sciences 42 (2005) 933–949.
[9] D. Falleti, L. Ethridge, A method for predicting cracking in waste glass canisters, Nuclear and Chemical Waste Management 8 (1988) 123–133.
[10] J. Fortin, Y. Guéguen, A. Schubnel, Effects of pore collapse and grain crushing on ultrasonic velocities and v_p/v_s, Journal of Geophysical Research 112 (2007) B08207.
[11] L. Freund, Dynamic Fracture Mechanics, Cambridge University Press, New York, 1984.
[12] J. Frotin, A. Schubnel, Y. Guéguen, Elastic wave velocities and permeability evolution during compaction of bleurswiller sandstone, International Journal of Rock Mechanics and Mining Sciences 42 (2005) 873–889.
[13] P. Frugier, S. Gin, Y. Minet, T. Chave, B. Bonin, N. Godon, J. Lartigue, P. Jollivet, A. Ayral, L.D. Windt, G. Santarini, Son68 nuclear glass dissolution kinetics: current state of knowledge and basis of the new Graal model, Journal of Nuclear Materials 380 (2008) 8–21.
[14] J. Goodier, Concentration of stress around spherical and cylindrical inclusions and flaws, Journal of Applied Mechanics 55 (1933) A39.
[15] V. Grechka, M. Kachanov, Effective elasticity of cracked rocks: a snapshot of the work in progress, Geophysics 71 (2006) W45–W48.
[16] S. Gross, J. Fineberg, M. Marder, W. McCormick, H. Swinney, Acoustic emissions from rapidly moving cracks, Physical Review Letters 71 (1993) 3162–3165.
[17] K. Hadley, Comparison of calculated and observed crack densities and seismic velocities in westerly granite, Journal of Geophysical Research 81 (1976) 3484–3493.
[18] M. Kachanov, Continuum model of medium with cracks, Journal of the Engineering Mechanics Division (1980) 1039–1051.
[19] M. Kachanov, Elastic solids with many cracks and related problems, Advances in Applied Mechanics 30 (1993) 259–445.
[20] M. Kachanov, Elastic solids with many cracks and related problems, Advances in Applied Mechanics 30 (1994) 259–445.
[21] H. Kamizono, M. Senoo, Thermal shock resistance of a simulated high-level waste glass, Nuclear and Chemical Waste Management 4 (1983) 329–333.
[22] B. Lawn, Fracture of Brittle Solids, second ed., Cambridge University Press, New York, 1993.
[23] F. Lehner, M. Kachanov, On modelling of 'winged' cracks forming under compression, International Journal of Fracture 77 (1996) R69–R75.

[24] Z. Lu, K. Nomura, A. Sharma, W. Wang, C. Zhang, A. Nakano, R. Kalia, P. Vashishta, Dynamics of wing cracks and nanoscale damage in glass, Physical Review Letters 95 (2005) 135501.
[25] G. Mavko, T. Mukerji, J. Dvorkin, The Rock Physics Handbook, Cambridge University Press, Cambridge, 1998.
[26] M. Meyers, R. Armstrong, H. Kirchner, J. Willis, J. Rice, D. Barnett, G. Thomas, J. Gilman, A. Argon, L. Anand, P. Veyssière, J. Knott, A. Boccaccini, B. Adams, J. Weertman, R. Ritchie, Mechanics and Materials – Fundamentals and Linkages, Wiley-Interscience, 1999.
[27] J. Perez, J. Westsik, Effects of cracks on glass leaching, Nuclear and Chemical Waste Management 2 (1981) 165–168.
[28] K. Ravi-Chandar, W. Knauss, An experimental investigation into dynamic fracture: I. Crack initiation and arrest, International Journal of Fracture 25 (1984) 247–262.
[29] K. Ravi-Chandar, W. Knauss, An experimental investigation into dynamic fracture: II. Microstructural aspects, International Journal of Fracture 26 (1984) 65–80.
[30] K. Ravi-Chandar, W. Knauss, An experimental investigation into dynamic fracture: III. On steady-state crack propagation and crack branching, International Journal of Fracture 26 (1984) 141–154.
[31] K. Ravi-Chandar, W. Knauss, An experimental investigation into dynamic fracture: IV. On the interaction of stress waves with propagating cracks, International Journal of Fracture 26 (1984) 189–200.
[32] K. Sakaue, S. Yoneyama, M. Takashi, Study on crack propagation behavior in a quenched glass plate, Engineering Fracture Mechanics 76 (2009) 2001–2024.
[33] C. Sammis, M. Ashby, The failure of brittle porous solids under compressive stress states, Acta Metallurgica 34 (1986) 511–526.
[34] J. Sarout, Y. Guéguen, Elastic wave velocities evolution in experimentally deformed anisotropic shales – Part II: Modeling results, Geophysics 73 (2008) D91.
[35] S. Sato, K. Asakura, H. Furuya, Microstructure of high-level radioactive waste glass heavily irradiated in a high-voltage electron microscope, Nuclear and Chemical Waste Management 4 (1983) 147–151.
[36] C. Sayers, M. Kachanov, Microcracks-induced elastic wave anisotropy of brittle rocks, Journal of Geophysical Research 100 (1995) 4149–4156.
[37] A. Schubnel, Y. Guéguen, Dispersion and anisotropy of elastic waves in cracked rocks, Journal of Geophysical Research 108 (B2) (2003).
[38] A. Schubnel, E. Walker, B. Thompson, J. Fortin, Y. Guéguen, R. Young, Transient creep, aseismic damage and slow failure in carrara marble deformed across the brittle-ductile transition, Geophysical Research Letters 33 (2006) L17301.
[39] I. Sevostianov, M. Kachanov, Explicit cross-properties correlations for anisotropic two-phase composite materials, Journal of the Mechanics and Physics of Solids 50 (2002) 253–282.
[40] B. Thompson, R. Young, D. Lockner, Observations of premonitory acoustic emission and slip nucleation during a stick slip experiment in smooth faulted westerly granite, Geophysical Research Letters 32 (2005) L10304.
[41] B. Thompson, R. Young, D. Lockner, Fracture in westerly granite under ae feedback and constant strain rate loading: nucleation, quasi-static propagation, and the transition to unstable fracture propagation, Pure and Applied Geophysics 163 (2006) 995–1019.
[42] S. Vinciguerra, C. Trovato, P. Meredith, P. Benson, Relating seismic velocities, thermal cracking and permeability in mt. etna and iceland basalts, International Journal of Rock Mechanics and Mining Sciences 42 (2005) 900–910.
[43] J. Walsh, The effect of cracks on the compressibility of rocks, Journal of Geophysical Research 70 (1965) 381–389.
[44] H. Yin, Acoustic Velocity and Attenuation of Rocks: Isotropy, Intrinsic Anisotropy, and Stress Induced Anisotropy, Ph.D. Thesis, Stanford University, Stanford, USA, 1992.